

Journal of Materials Chemistry A

Accepted Manuscript



This is an *Accepted Manuscript*, which has been through the Royal Society of Chemistry peer review process and has been accepted for publication.

Accepted Manuscripts are published online shortly after acceptance, before technical editing, formatting and proof reading. Using this free service, authors can make their results available to the community, in citable form, before we publish the edited article. We will replace this *Accepted Manuscript* with the edited and formatted *Advance Article* as soon as it is available.

You can find more information about *Accepted Manuscripts* in the [Information for Authors](#).

Please note that technical editing may introduce minor changes to the text and/or graphics, which may alter content. The journal's standard [Terms & Conditions](#) and the [Ethical guidelines](#) still apply. In no event shall the Royal Society of Chemistry be held responsible for any errors or omissions in this *Accepted Manuscript* or any consequences arising from the use of any information it contains.



ARTICLE

Fabrication of a ternary CdS/ZnIn₂S₄/TiO₂ heterojunction for enhancing photoelectrochemical performance: Effect of cascading electron-hole transfer†

Received 00th January 20xx,
Accepted 00th January 20xx

DOI: 10.1039/x0xx00000x

www.rsc.org/

Mahadeo A. Mahadik, Pravin S. Shinde, Min Cho* and Jum Suk Jang*

A novel, three-dimensional, ternary CdS/ZnIn₂S₄/TiO₂ heterojunction has been fabricated via a three-step facile hydrothermal method. In this structure, three-dimensional TiO₂ nanorods were directly grown on conductive fluorine-doped tin oxide (FTO) substrates. Next, to form a ternary heterojunction of CdS/ZnIn₂S₄/TiO₂, ZnIn₂S₄ nanosheets were designed on the TiO₂ nanorods and sensitized by CdS nanograins. A systematic photoelectrochemical study shows that the photocurrent density of the ternary heterojunction architecture is as high as 1.4 mA cm⁻² at a potential of 0.1 V versus Ag/AgCl (at optimized conditions). A more detailed study shows that the photocurrent density is more than two times higher than a single CdS/TiO₂ heterojunction (0.615 mA cm⁻²) and three times higher than that of ZnIn₂S₄/TiO₂ (at 0.1 V vs. Ag/AgCl). This excellent photoelectrochemical performance is ascribed to the way that the structure of the TiO₂ nanorods synergistically cascades with ZnIn₂S₄ and CdS, which allows for the absorption of a wider portion of the solar spectrum and improves the effective separation of the generated electron-hole pairs. Electrochemical impedance (EIS) studies also reveal the significant changes in both the interface resistance and the charge transfer resistance of the CdS/ZnIn₂S₄/TiO₂ heterostructure. This can be attributed to the efficient hierarchical cascading that occurs during the electron-hole transfer from the excited CdS to TiO₂ through the enlarged interface of ZnIn₂S₄ upon visible light illumination.

Introduction

Recently, a major technological challenge facing nanoscience and nanotechnology is the production of clean and renewable sources of energy. Considering the importance of nanostructured photocatalysts, researchers are trying to architect different nanostructured building blocks with interesting morphologies and tunable properties for various innovative clean energy applications like hydrogen generation. H₂S is a toxic, malodorous, corrosive nature that occurs widely in natural gas and is also produced in large amounts by the coal and petroleum industries as an undesirable byproduct.¹ With this in mind, the photocatalytic splitting of H₂S and water into hydrogen using solar energy is a potentially clean and renewable source of hydrogen fuel and is an attractive and sustainable solution to current energy problems.² Photoelectrochemical cells are effective devices for converting solar light into hydrogen energy by water splitting; these devices use photoelectrodes that are composed of semiconductors. In the last few years, photocatalysis research

has taken advantage of oxide semiconductors due to their unique properties.³⁻⁶ More recently, attention has been focused on hydrogen generation from natural sources, like water, by irradiating single semiconductors.⁷ Among the various oxide semiconductors that have been studied, titanium dioxide (TiO₂) has attracted significant interest due to its chemically stable properties. However, because of its large energy bandgap (3.0-3.2 eV), it absorbs only about 2–4 % of solar light in the UV region, preventing its efficient visible light absorption. To improve the solar spectrum efficiency, various narrow bandgap semiconductors have been considered as promising sensitizers for TiO₂ to enhance the utilization of sunlight for energy production.⁸ Among various semiconductor sensitizers, II–VI compound semiconductors (like CdS)^{9, 10} are widely used to sensitize nanocrystalline TiO₂; these materials are desirable due to their size-tunable optical properties.¹¹ Serpone *et al.* were the first group to demonstrate that the coupling of two semi-conductors (e.g., CdS and TiO₂) leads to an inter-particle electron transfer process, which yields improved dihydrogen production during the photo-reduction of water in the presence of hydrogen sulfide as a sacrificial agent.^{12, 13} Biswas and Chen reported that CdS is one of the most extensively studied nanocrystalline semiconductor materials because of its suitable bandgap, long lifetime, important optical properties, outstanding stability, and the fact that its energy level matches with that of TiO₂.^{14, 15} Although CdS-sensitized TiO₂ can significantly expand the absorption spectra range, the low interfacial area between these two

Division of Biotechnology, Advanced Institute of Environmental and Bioscience, College of Environmental and Bioresource Sciences, Chonbuk National University, Iksan 570-752, Republic of Korea,

*Corresponding authors. Tel.: +82 63 850 0846; fax: +82 63 850 0834.

E-mail addresses: jangjs75@jbnu.ac.kr (J.S. Jang), cho317@jbnu.ac.kr (Min Cho).

† Electronic Supplementary Information (ESI) available: [Reaction mechanism, XPS survey spectra, FESEM, and Tauc plots]. See DOI: 10.1039/x0xx00000x

ARTICLE

Journal of Materials chemistry A

semiconductors can influence the separation efficiency of electrons and holes; therefore, interfacial optimization of the heterogeneous junction is necessary to further improve the photoelectrochemical conversion efficiency. To solve this problem, the appropriate semiconductor heterostructure or composite (with matching band potentials) must be chosen. This selection should allow for the efficient separation and migration of the photoinduced electrons and holes.¹⁶ Thus, the development of new, visible light nanostructured photocatalysts has become an imperative topic in current photocatalysis research. Recently, ternary sulfide ZnIn_2S_4 with a 2D layer structure (an II-III₂-VI₄ semiconductor) has attracted increased attention due to its potential applications in various fields such as photoconduction and charge storage.¹⁷ The 2D structure of ZnIn_2S_4 promotes efficient charge migration across the semiconductor/photoelectrode interface due to increased photon-semiconductor interaction via multiple reflections and scattering at the semiconductor/electrolyte interface.¹⁸ However, some of the photocatalysts that are visible light-active, like $\text{ZnIn}_2\text{S}_4/\text{TiO}_2$, are unable to perform the water reduction reaction due to the insufficient over-potential supplied by the conduction band. Hence, by considering the synergistic effects between different semiconductors, heterostructure photoanodes with enhanced photoelectrochemical performance can be produced.¹⁹ Fan *et al.* recently fabricated ternary $\text{TiO}_2/\text{RGO}/\text{Cu}_2\text{O}$ heterostructure by using a reduced graphene oxide (RGO) layer between TiO_2 and Cu_2O , which exhibited significant photocurrent improvement compared to the pristine TiO_2 .²⁰ Huang *et al.* also fabricated ternary $\text{Cu}_2\text{O}/\text{CuO}/\text{TiO}_2$ nanowire arrays on Au substrates. The Cu_2O layer on CuO/TiO_2 was found to prevent the photo-corrosion and enhance the overall photocurrent of CuO .²¹ However, the efficiency of these metal oxide-based heterostructure catalysts is still low and requires further improvement. In contrast to metal oxide photocatalysts, many metal sulfides have narrow bandgaps that correspond to the absorption of visible light. Hence, it has been reported that constructing a heterostructure is an effective method to improve the photocatalytic activity because heterostructures have proven to have a great effect on electron transfer.^{22, 23} As far as we know, there have not yet to be any corresponding reports about photoanodes built from TiO_2 , ZnIn_2S_4 , and CdS . Therefore, it will be a challenge to design and fabricate this type of heterostructure photoanode for enhanced photoelectrochemical performance under visible light irradiation.

In the present work, which is based on the outstanding features of CdS and ZnIn_2S_4 , we have for the first time systematically designed and fabricated a chemically stable ternary $\text{CdS}/\text{ZnIn}_2\text{S}_4/\text{TiO}_2/\text{FTO}$ architecture. In this structure, both the ZnIn_2S_4 and CdS layers allow for cascading electron-hole transfer. First, TiO_2 nanorods were synthesized by a hydrothermal method on fluorine-doped tin oxide conductive glass (FTO) substrates. It should be noted that the dynamics of charge separation and transport are limited in TiO_2 due to its low electron mobility ($0.1\text{--}1\text{ cm}^2\text{ V}^{-1}\text{ s}^{-1}$). Secondly, we deposited ZnIn_2S_4 nanosheets, with a fascinating design, on

the surface of TiO_2 nanorods through a hydrothermal method. This nanosheet structure can greatly increase the surface area and provide more sites for charge separation and transfer. Finally, the CdS layer was deposited onto the surface of ZnIn_2S_4 via low temperature hydrothermal deposition to further increase light absorption in the heterostructure. The ternary $\text{CdS}/\text{ZnIn}_2\text{S}_4/\text{TiO}_2/\text{FTO}$ architecture can present excellent photoelectrochemical performance compared to CdS/TiO_2 and $\text{ZnIn}_2\text{S}_4/\text{TiO}_2$ photoanodes. Photoelectrochemical impedance (EIS) studies were performed to investigate the origin of charge separation and the effective electron-hole transport observed in the $\text{CdS}/\text{ZnIn}_2\text{S}_4/\text{TiO}_2/\text{FTO}$ architecture. The significantly changed interface resistance and the charge transfer resistance of the $\text{CdS}/\text{ZnIn}_2\text{S}_4/\text{TiO}_2$ heterostructure can be attributed to the effective hierarchical electron-hole transfer cascade system.

Experimental

Reagents and chemicals

Titanium butoxide ($\text{Ti}(\text{OCH}_2\text{CH}_2\text{CH}_2\text{CH}_3)_4$), HCL (36%), zinc sulfate heptahydrate ($\text{ZnSO}_4\cdot 7\text{H}_2\text{O}$), indium chloride tetrahydrate ($\text{InCl}_3\cdot 4\text{H}_2\text{O}$), thioacetamide (CH_3CSNH_2), and cadmium nitrate tetrahydrate ($\text{Cd}(\text{NO}_3)_2\cdot 4\text{H}_2\text{O}$) were analytical reagents and used as-received. Distilled water was used to prepare all of the solutions.

Synthesis of TiO_2 nanorods on FTO

Hydrothermal synthesis of TiO_2 on FTO glass was prepared by a simple method, as reported by Cao *et al.*²⁴ 30 mL of distilled water was mixed with 30 mL of concentrated hydrochloric acid (36% by weight) and stirred for 5 min at ambient temperature. Next, 1 mL of titanium butoxide was added to the above solution and stirred for 30 min. This solution was transferred into a Teflon-lined stainless steel autoclave filled to 60% of its capacity. Two pieces of FTO glass substrates, with dimensions of 10 mm × 25 mm, were ultrasonically cleaned in acetone, ethanol, and distilled water (in sequence) for 10 min each, dried under N_2 flow, and placed into the Teflon cylinder. The autoclave was sealed and maintained at 150 °C for 4 h and cooled naturally to room temperature. Finally, a white layer of TiO_2 formed on the FTO substrates, which were thoroughly washed with water and dried at room temperature.

Hydrothermal synthesis of ZnIn_2S_4 and CdS layers on TiO_2/FTO photoanodes

Hydrothermal synthesis of ZnIn_2S_4 on $\text{TiO}_2/\text{FTO}/\text{glass}$ and bare FTO/glass was completed by a simple method, as reported by Peng *et al.*²⁵ The $\text{ZnSO}_4\cdot 7\text{H}_2\text{O}$ (1.6 mmol), $\text{InCl}_3\cdot 4\text{H}_2\text{O}$ (3.2 mmol), and $\text{C}_2\text{H}_5\text{NS}$ (6.4 mmol) were added into 50 mL of distilled water, ultrasonicated for 5 min, and stirred for 30 min. After that, the solution was transferred into a Teflon-lined stainless steel autoclave (which was filled to 60% of its capacity), sealed, maintained at 160 °C for 2 h, and cooled naturally to room temperature. Finally, a ZnIn_2S_4 film (a light green homogeneous layer) was deposited on the FTO and

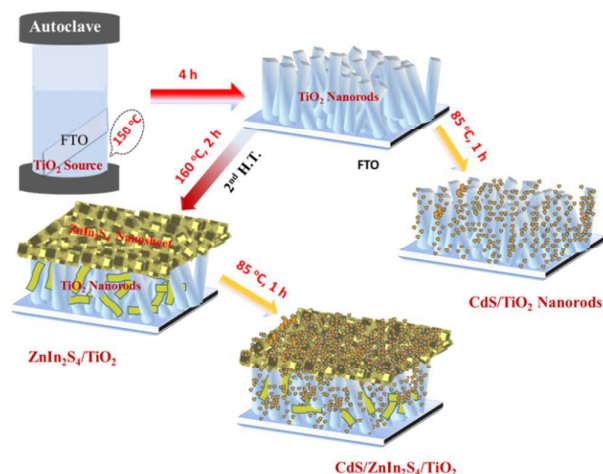


Fig. 1 Schematic of facile hydrothermal syntheses for TiO_2/FTO , $\text{ZnIn}_2\text{S}_4/\text{TiO}_2/\text{FTO}$, and $\text{CdS}/\text{ZnIn}_2\text{S}_4/\text{TiO}_2/\text{FTO}$ heterostructure photoanodes.

TiO_2/FTO glass substrates. After deposition, the ZnIn_2S_4 films were thoroughly washed with ethanol and dried at room temperature. To deposit the CdS layer on TiO_2/FTO and $\text{ZnIn}_2\text{S}_4/\text{TiO}_2/\text{FTO}$, 0.01 M cadmium nitrate tetra-hydrate ($\text{Cd}(\text{NO}_3)_2 \cdot 4\text{H}_2\text{O}$) was added to the 1 M ammonia solution and stirred for 5 min. Then, 0.05 M thiourea was added into the above solution and again stirred for 5 min. The resulting solution was transferred into 20 mL glass vials; one sample each of the FTO, TiO_2/FTO , and $\text{ZnIn}_2\text{S}_4/\text{TiO}_2/\text{FTO}$ glass substrates was placed into these vials at an angle against the wall of the vial with the conducting side facing down. The vials were sealed, maintained at 85 °C for 1 h, and cooled naturally to room temperature. Finally, a yellowish layer of CdS was formed on the FTO, TiO_2/FTO , and $\text{ZnIn}_2\text{S}_4/\text{TiO}_2/\text{FTO}$ substrates, which were then thoroughly washed with water and dried at room temperature. The possible reaction mechanism for the formation of CdS is provided in the Supporting Information. The schematic of the facile hydrothermal syntheses of TiO_2/FTO , $\text{ZnIn}_2\text{S}_4/\text{TiO}_2/\text{FTO}$, and $\text{CdS}/\text{ZnIn}_2\text{S}_4/\text{TiO}_2/\text{FTO}$ thin films is shown in Fig. 1.

Characterization

Structural analysis of $\text{CdS}/\text{ZnIn}_2\text{S}_4/\text{TiO}_2/\text{FTO}$ thin films was performed using X-ray diffraction patterns (XRD) recorded with a Bruker D8 Focus Diffraction System using a $\text{Cu K}\alpha$ source ($\lambda = 0.154178$ nm) in the 2θ range between 20° and 80°. X-ray photoelectron spectroscopy (XPS) was used for identification of the chemical states and elemental quantification. XPS analysis was performed with a PHI Quantera II XPS spectrometer equipped with a monochromatic $\text{Al K}\alpha$ X-ray source ($h\nu = 1486.6$ eV). The morphologies of the deposited films were examined using a field emission scanning electron microscope (FESEM) (SUPRA 40VP, Carl Zeiss, Germany) equipped with an X-ray energy dispersive spectrometer (EDX). Transmission electron microscopy (TEM) was performed with a JEOL JEM-3100F transmission electron microscope operating at 200 kV. UV-Vis-DRS spectra were measured using a dual-

beam spectrophotometer (Shimadzu, UV-2600 series) in the wavelength range of 300–800 nm.

Photoelectrochemical measurements

Photoelectrochemical (PEC) measurements were performed in a 0.1 M Na_2S + 0.02 M Na_2SO_3 electrolyte solution. The working electrodes were illuminated using a simulated sunlight source under 100 mW cm^{-2} irradiation. The photocurrent measurements (J – V) were carried out with a conventional three-electrode electrochemical cell; Pt wire and Ag/AgCl (saturated KCl) were used as the counter and reference electrodes, respectively. A portable potentiostat (COMPACTSTAT.e, Ivium, Netherlands) equipped with an electrochemical interface and impedance analyzer was employed for EIS measurements. The experimental EIS data were fitted to the suitable equivalent circuit model using the Z View (Scribner Associates Inc.) program. The photoelectrochemical hydrogen production experiments were performed in a closed reactor at a 0.1 V bias vs. Ag/AgCl with a $\text{CdS}/\text{ZnIn}_2\text{S}_4/\text{TiO}_2/\text{FTO}$ photoanode and Pt as the counter electrode. Evolved hydrogen at the platinum (Pt) counter electrode was analyzed via gas chromatography with TCD, a molecular sieve 5-Å column, and N_2 as the carrier gas.

Results and discussion

Structural characterization of the TiO_2 , $\text{ZnIn}_2\text{S}_4/\text{TiO}_2$, CdS/TiO_2 , and $\text{CdS}/\text{ZnIn}_2\text{S}_4/\text{TiO}_2$ heterostructure thin films

X-ray diffraction (XRD) patterns of the pristine TiO_2 nanorod array, $\text{ZnIn}_2\text{S}_4/\text{TiO}_2$, the CdS/TiO_2 nanostructure, and the ternary $\text{CdS}/\text{ZnIn}_2\text{S}_4/\text{TiO}_2$ heterostructure are shown in Fig. 2. The TiO_2 nanorods array grown on FTO-coated glass substrates (Fig. 2b) had a tetragonal rutile structure (JCPDS 02–0494). Hydrothermal growth provides only the rutile phase instead of the other phases (i.e., anatase and brookite) of TiO_2 on FTO. This may be attributed to the fact that both rutile and SnO_2 have nearly identical lattice parameters ($a = 4.594$, $c = 2.958$ Å and $a = 4.737$, $c = 3.185$ Å, respectively).

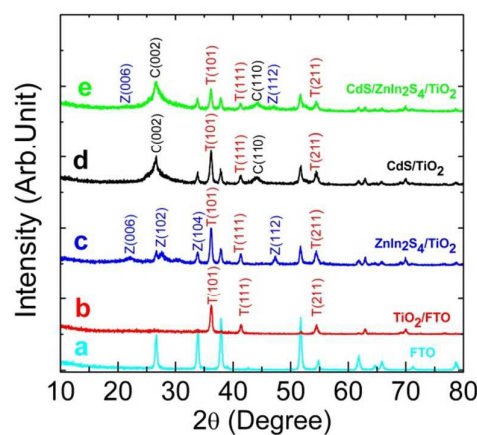


Fig. 2 XRD patterns of (a) FTO glass, (b) TiO_2/FTO , (c) $\text{CdS}/\text{TiO}_2/\text{FTO}$, (d) $\text{ZnIn}_2\text{S}_4/\text{TiO}_2/\text{FTO}$, and (e) $\text{CdS}/\text{ZnIn}_2\text{S}_4/\text{TiO}_2/\text{FTO}$.

Besides the rutile peaks (T (101), T (111), and T (211)) of TiO_2 , all of the other peaks in the XRD pattern of TiO_2/FTO are mainly due to the FTO substrates (Fig. 2a). Similar results were obtained by Xie.²⁶ Alternatively, due to the lattice mismatch between anatase and brookite with FTO, a very high activation energy barrier is formed, which cannot be overcome during the hydrothermal synthesis method because of the low temperature. $\text{ZnIn}_2\text{S}_4/\text{TiO}_2/\text{FTO}$ (Fig. 2c) shows additional diffraction peaks at $2\theta = 21.6^\circ$, 27.8° , 33.9° , and 47.28° , which correspond to the Z(006), Z(102), Z(104), and Z(112) crystal planes of hexagonal ZnIn_2S_4 , respectively (space group: $P63mc$, a and $b = 3.85(2) \text{ \AA}$, $c = 24.68(4) \text{ \AA}$, JCPDS 72-0773).^{27, 28} Compared to TiO_2/FTO thin films, the $\text{CdS}/\text{TiO}_2/\text{FTO}$ shows more diffraction peaks. These become more distinct at 2θ of 26.5° and 44.05° , which correspond to the diffractions of the (002) and (110) planes for the hexagonal wurtzite phase of CdS (JCPDS 89-2944). However, in the case of the ternary $\text{CdS}/\text{ZnIn}_2\text{S}_4/\text{TiO}_2$ heterostructure (Fig. 2e), suppressed peak intensity with a slight shift in the peak positions of ZnIn_2S_4 and TiO_2 compared to Fig. 2d. This confirms that the CdS nanograins are distributed randomly on the surface of the $\text{ZnIn}_2\text{S}_4/\text{TiO}_2/\text{FTO}$ structure and that a small amount is also filled in the interstices.

To further confirm the composition, the valance states of $\text{ZnIn}_2\text{S}_4/\text{TiO}_2$ (ZT) and $\text{CdS}/\text{ZnIn}_2\text{S}_4/\text{TiO}_2$ (CZT) heterostructure films are characterized by XPS measurement. The survey XPS spectra (Fig. S1, Supporting Information) depict the presence of Cd, Zn, In, Ti, O, and S elements in the samples. Meanwhile, high-resolution XPS peaks of $\text{Cd}3d$, $\text{S}2p$, $\text{Zn}2p$, and $\text{In}3d$ are investigated in detail. All of the peaks are calibrated using C 1s as the reference peak at 284.6 eV. The $\text{Cd}3d$ high-resolution spectrum (Fig. 3a) has two sharp peaks at 411.7 eV ($\text{Cd}3d_{3/2}$) and 404.9 eV ($\text{Cd}3d_{5/2}$), which are attributed to the Cd^{2+} state in CdS . The typical splitting energy difference of $\text{Cd}3d_{5/2}$ and $\text{Cd}3d_{3/2}$ is 6.8 eV, which corresponds to the presence of $\text{Cd}3d$ with an oxidation state of +2 at the surface.^{29, 30}

Fig. 3b shows an asymmetric $\text{S}2p$ peak that can be deconvoluted into two peaks at 162.61 eV ($\text{S}2p_{1/2}$) and 161.39 eV ($\text{S}2p_{3/2}$), which also correspond well with the respective literature values.^{31,32} This suggests the presence of divalent sulfide ions (S^{2-}) in CdS and ZnIn_2S_4 .²⁵ XPS reveals the atomic ratio of Cd/S to be 1.3. A deviation from the 1:1 atomic ratio of Cd/S is consistent with the observed shift in binding energy values of $\text{Cd}3d$ and $\text{S}3p$, and is considered to be due to the presence of S^{2-} between the ZnIn_2S_4 and CdS .³³ The high-resolution XPS spectra of $\text{Zn}2p$ in ZT and CZT, shown in Fig. 3c, shows that the signals of $\text{Zn}2p$ occur at binding energies of 1021.67 eV ($\text{Zn}2p_{3/2}$) and 1045.12 eV ($\text{Zn}2p_{1/2}$). This confirms that Zn is present in the Zn^{2+} state, which is in good agreement with the results obtained by Hou et al.³⁴ In the high-resolution XPS spectra of $\text{In}3d$, two sharp peaks are observed at 444.6 eV ($\text{In}3d_{5/2}$) and 452.27 eV ($\text{In}3d_{3/2}$) (Fig. 3d); these correspond to In^{3+} . Thus, the presence of Zn, In and S having chemical states of 2+, 3+, and 2- confirms the formation of ZnIn_2S_4 product. However, in the case of the CZT film, the XPS signals of $\text{In}3d$ and $\text{Zn}2p$ are much less intense (compared to the ZT film), which confirms the occurrence of CdS on the surface of ZT. These results are in good agreement with the XRD results.

Figs. 4 (a-j) depict the TEM images, element mappings, and EDX spectrum of $\text{CdS}/\text{ZnIn}_2\text{S}_4/\text{TiO}_2$ heterostructure thin films.

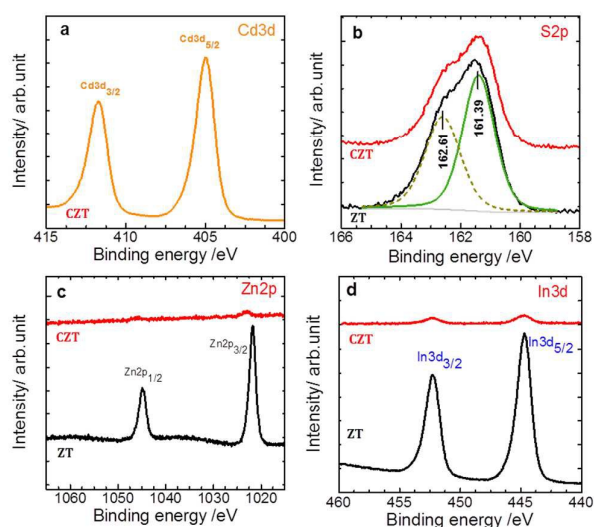


Fig. 3 XPS spectra of (a) $\text{Cd}3d$, (b) $\text{S}2p$, (c) $\text{Zn}2p$, and (d) $\text{In}3d$ for $\text{CdS}/\text{ZnIn}_2\text{S}_4/\text{TiO}_2/\text{FTO}$ heterostructure photoanodes.

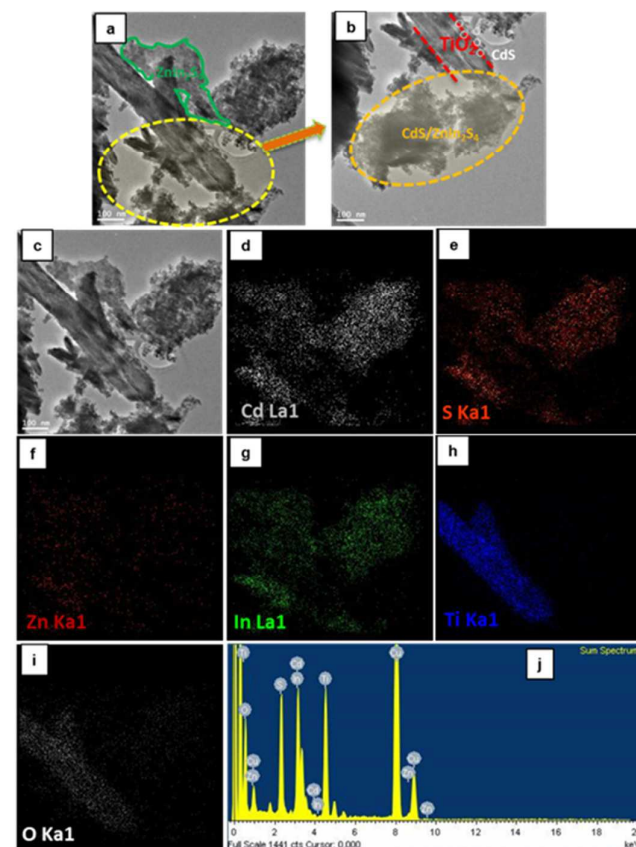


Fig. 4 (a-b) TEM images of the $\text{CdS}/\text{ZnIn}_2\text{S}_4/\text{TiO}_2$ photoanode and (c) the element distribution maps of a scanning TEM (STEM) images. The presence of (d) Cd, (e) S, (f) Zn, (g) In, (h) Ti, and (i) O elements on the $\text{CdS}/\text{ZnIn}_2\text{S}_4/\text{TiO}_2$ photoanode. (j) A typical EDX spectrum of $\text{CdS}/\text{ZnIn}_2\text{S}_4/\text{TiO}_2$.

TEM characterization was carried out by scratching the CdS/ZnIn₂S₄/TiO₂ film from the FTO glass. Careful scrutiny of the surface revealed that nano-scale CdS layers were successfully coated on ZnIn₂S₄ (orange dotted circle in Fig. 4b) and TiO₂ (small white circles in Fig. 4b) to form a multi-heterojunction architecture. This CZT structure can absorb the maximum amount of visible light and provides multi-steering charge transfer, which can enhance the concentration of photogenerated charge carriers and increase the photoelectrochemical performance. Furthermore, the elemental composition of CdS/ZnIn₂S₄/TiO₂ was investigated by EDX mapping images. Figs. 4 (c-h) show scanning TEM (STEM) images and several elemental mapping images; the STEM measurement indicates that the TiO₂ nanorods clearly contrast with and possess clear interfaces from the ZnIn₂S₄ and CdS layers. However, the homogeneous distribution of Cd, S, Zn, and In (Fig. 4d-g) suggests that CdS is grown homogeneously onto the ZnIn₂S₄ nanosheets. The width of the Ti and O mapping images are smaller compared to the others, which also provides direct proof that the ZnIn₂S₄ and CdS layers are present on the surface of the TiO₂ nanorods. Thus, the elemental mapping analysis of CdS/ZnIn₂S₄/TiO₂ confirms the coexistence of CdS, ZnIn₂S₄, and TiO₂, which are evenly distributed in the CdS/ZnIn₂S₄/TiO₂ architecture. Additionally, the coexistence of CdS, ZnIn₂S₄, and TiO₂ is also confirmed from TEM EDX analysis (Fig. 4j). The stoichiometric formation of CdS is confirmed from the EDX data (Table S1) and agrees well with the XPS data in Fig. 3. As seen from Table S1, the atomic % values of 0.29 for Zn, 3.22 for In, and 25.16 for S were observed for CZT sample. The higher atomic % of S is due to the sharing of S²⁻ ions between CdS and ZnIn₂S₄. At times, it is very difficult to realize the exact chemical composition of the heterojunction involving ternary compounds from EDS. Although EDS reveals zinc deficiency, a phase-pure formation of ZnIn₂S₄ is previously confirmed from the XRD and XPS analyses. Thus, TEM elemental mapping and EDX results reveal the homogeneous distribution of Cd and S as well as Zn, In, and S in the composition.

Morphological study

The surface morphologies of the as-synthesized TiO₂, ZnIn₂S₄/TiO₂, and CdS/ZnIn₂S₄/TiO₂ are depicted in Fig. 5. FESEM images of TiO₂/FTO show that the entire surface of the FTO-coated glass substrate is uniformly covered with ordered TiO₂ nanorods. The tetragonal TiO₂ nanorods are typically 100 to 175 nm in diameter, have square top facets, and consist of many small grids. After the second hydrothermal process, the top surface of the TiO₂ nanorods array is covered by a ZnIn₂S₄ thin film nanosheet with an average thickness about 10 nm, as shown in the Fig. 5b. The cross-sectional image of ZnIn₂S₄/TiO₂ indicates that the ZnIn₂S₄ nanosheets are distributed randomly on the surface and within the interstices of the TiO₂ nanorods, thereby reducing the gaps between TiO₂ nanorods. However, in CdS/TiO₂ (Figure S2), the top and cross-sectional views of the CdS/TiO₂ bilayer film show spherical grains of CdS attached to TiO₂ nanorods up to the FTO substrates; this provides a

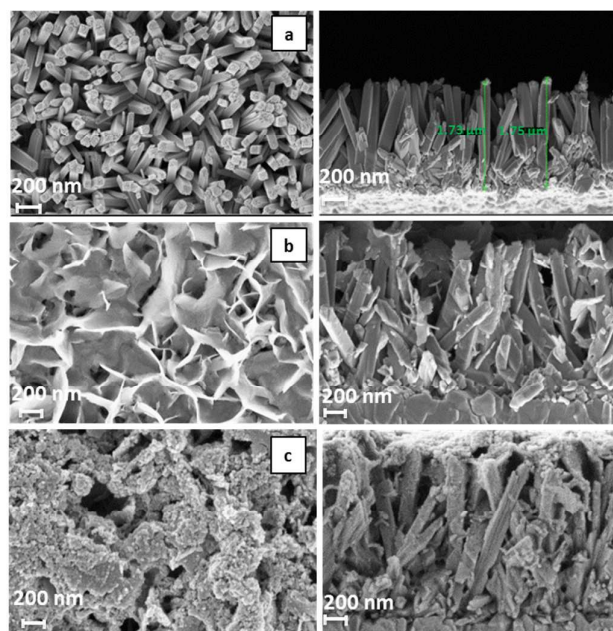


Fig. 5 SEM top (left) and cross-sectional (right) images of (a) TiO₂/FTO, (b) ZnIn₂S₄/TiO₂/FTO, and (c) CdS/ZnIn₂S₄/TiO₂/FTO.

maximum surface with little aggregation of the CdS grains on the top surface of TiO₂. Additionally, the surface morphology of pristine ZnIn₂S₄ and CdS on FTO shows ZnIn₂S₄ films with uniform nanosheets that have an average sheet thickness of about 20 nm. However, the CdS nanograins on FTO possess a low thickness (near 64 nm), as shown in Fig. S3 (Supporting Information). The SEM top and cross-sectional views of CdS/ZnIn₂S₄/TiO₂ indicate that a small amount of CdS nanograins are incorporated into the lattice of ZnIn₂S₄/TiO₂ while a majority of CdS nanograins remain on the surface of ZnIn₂S₄ nanosheets; this adds to the thickness of the photoanode and increases the surface area, which enables prospective applications in energy conversion devices as well as photocatalysis. The presence of CdS on the surface of ZnIn₂S₄/TiO₂ is also confirmed from the XPS results.

Optical properties

The UV-Vis diffuse reflectance spectra and Tauc plots of the TiO₂, ZnIn₂S₄/TiO₂, CdS/TiO₂, and CdS/ZnIn₂S₄/TiO₂ samples are shown in Fig. 6. The optical absorption of the pristine TiO₂ is found to be in the wavelength range from 300 to 410 nm. However, due to the dark yellowish color of CdS in the CdS/TiO₂ and CdS/ZnIn₂S₄/TiO₂ nanostructured films, the absorption edges were shifted in the visible region of the solar spectrum to about 515 and 522 nm (2.39 and 2.37 eV, respectively) relative to the pristine TiO₂ (3.2 eV)³⁵ and ZnIn₂S₄/TiO₂ (2.97 eV) thin films. This is in good agreement with the results obtained by Chi³⁶ and Dang³⁷. Additionally, the Tauc plots^{38,39} of pristine CdS/FTO and ZnIn₂S₄/FTO are shown in Fig. S4.

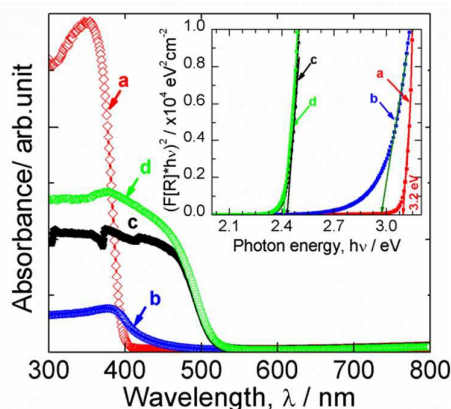


Fig. 6 UV-Vis absorption spectra of (a) pristine TiO_2 , (b) $\text{ZnIn}_2\text{S}_4/\text{TiO}_2$, (c) CdS/TiO_2 , and (d) $\text{CdS}/\text{ZnIn}_2\text{S}_4/\text{TiO}_2$ photoanodes. Inset shows the corresponding Tauc plots.

In comparison to CdS/FTO and $\text{ZnIn}_2\text{S}_4/\text{FTO}$, it can be seen that the heterostructured photocatalysts (CdS/TiO_2 and $\text{ZnIn}_2\text{S}_4/\text{TiO}_2$) exhibit enhanced absorption in the visible range, implying that CdS and ZnIn_2S_4 are successfully deposited on the surface of the TiO_2 photoanodes. Furthermore, in the ternary $\text{CdS}/\text{ZnIn}_2\text{S}_4/\text{TiO}_2$ architecture, the CdS influences the energy bandgap of $\text{ZnIn}_2\text{S}_4/\text{TiO}_2$, which causes a shift in the absorption edge from 2.97 eV to 2.37 eV. Thus, the ternary architecture achieves the maximum light absorption in the 1D CdS nanograins and multiple light scattering in the 2D ZnIn_2S_4 nanosheets, which increases the interaction sites for generated charge carriers. This combination of light trapping and multiple interaction sites may contribute to the enhanced photocurrent in the $\text{CdS}/\text{ZnIn}_2\text{S}_4/\text{TiO}_2$ nanostructure.⁴⁰

Photoelectrochemical properties

To investigate the photocurrent response of TiO_2 upon addition of ZnIn_2S_4 and CdS layers, the photoelectrochemical (PEC) measurements were performed under visible-light irradiation. As shown in Fig. 7 (A), poor photocurrent density (J_{ph}) observed for TiO_2 nanorod electrode ($42 \mu\text{A cm}^{-2}$) can be easily explained by their poor optical light absorption properties as well as weak crystallinity that causes faster recombination of photogenerated electrons and holes.⁴¹ Upon formation of $\text{ZnIn}_2\text{S}_4/\text{TiO}_2$ heterostructure electrode, the J_{ph} value is remarkably improved to $369 \mu\text{A cm}^{-2}$. This enhancement can be attributed to the higher light absorption due to multiple light scattering resulting from ZnIn_2S_4 nanosheets and faster electron transfer due to higher conduction band position of ZnIn_2S_4 in comparison with TiO_2 .⁴² Relatively higher J_{ph} value for CdS/TiO_2 than $\text{ZnIn}_2\text{S}_4/\text{TiO}_2$ can be again ascribed to lower band gap energy as well as optimum coverage of visible light active nanoparticles on TiO_2 . Such coverage facilitates immediate interaction of nanoparticles with TiO_2 nanorods results in higher absorption of incident light leading to enhanced photoelectrochemical performance.⁴³ As a result, the electron-hole pairs are generated and separated effectively at the interface of the CdS/TiO_2 . These results are in agreement with the previous

literature.^{44,45} Interestingly, when ternary $\text{CdS}/\text{ZnIn}_2\text{S}_4/\text{TiO}_2$ heterostructure is formed, its J_{ph} value is about 60 times higher than pristine TiO_2 , 5.6 times higher than $\text{ZnIn}_2\text{S}_4/\text{TiO}_2$ and two times higher than the CdS/TiO_2 electrode. The significant improvement in the photocurrent of $\text{CdS}/\text{ZnIn}_2\text{S}_4/\text{TiO}_2$, compared to CdS/TiO_2 and $\text{ZnIn}_2\text{S}_4/\text{TiO}_2$ electrodes is due to the fact that ZnIn_2S_4 improves the photogenerated electron-hole separation through the efficient cascade charge transfer at the interface of CdS and TiO_2 as well as high surface area essential for interaction of light at the electrode-electrolyte interface. The cascade electron-transfer phenomenon results from the down-hill conduction band alignment (explained further from Fig.9). To study the electronic interactions occurring in the photoanodes, the photoresponse of electrodes with visible light switching (on and off) was measured. Fig. 7B depicts the corresponding photocurrent stability of the different electrodes, maintained after 300 s, and for the next four on-off light cycles. The $\text{CdS}/\text{ZnIn}_2\text{S}_4/\text{TiO}_2$ heterostructure exhibited relatively better photocurrent stability than CdS/TiO_2 . The prompt change observed between the on and off cycles indicates that the separation rate of photogenerated electron-hole pairs increased due to the formation of the heterojunction in CdS , ZnIn_2S_4 , and TiO_2 .⁴⁶ To determine the position of the band edges in ZnIn_2S_4 , CdS , and TiO_2 , the hydrothermally prepared photoanodes were characterized by Mott-Schottky (M-S) analysis. The V_{fb} can be calculated by extrapolating the linear region in the M-S plots ($1/C^2$ vs. V) to the voltage axis, as shown in Fig. 8. The shift in the V_{fb} values of CdS and ZnIn_2S_4 in the negative direction (as compared to TiO_2) might be attributed to the higher carrier concentration relative to that of the TiO_2 .⁴⁷

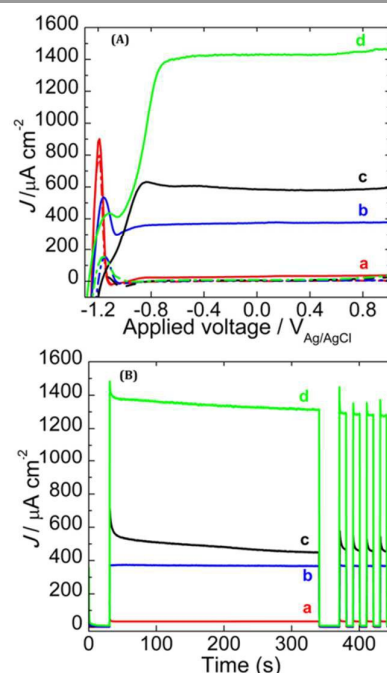


Fig. 7 (A) J - V curves and (B) photocurrent stability and transient photocurrent response to on-off cycles for (a) pristine TiO_2 , (b) $\text{ZnIn}_2\text{S}_4/\text{TiO}_2$, (c) CdS/TiO_2 , and (d) $\text{CdS}/\text{ZnIn}_2\text{S}_4/\text{TiO}_2$ photoanodes under 1sun light illumination (scan rate, 50 mV s^{-1}).

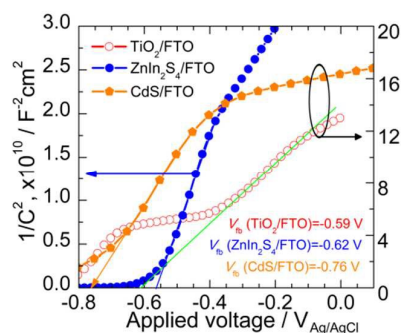


Fig. 8 Mott-Schottky plots of bare TiO_2 , ZnIn_2S_4 , and CdS on FTO measured in a 0.1 M Na_2S + 0.02 M Na_2SO_3 electrolyte.

A proposed cascade charge transfer mechanism in the ternary $\text{CdS}/\text{ZnIn}_2\text{S}_4/\text{TiO}_2$ heterojunction is depicted in Fig. 9. To understand the suggested mechanism, which is based on the experimental flat band potential data and the complementary band gap values of CdS , ZnIn_2S_4 , and TiO_2 , the conduction band (CB) and valence band (VB) positions can be plotted on an energy scale. The magnified view in Fig. 9 shows a possible cascading electron hole transfer.^{48,34,49} The CB of CdS is more negative than ZnIn_2S_4 , which is again more negative than TiO_2 . Subsequently, due to such down-hill energy scenario, the photogenerated electrons are quickly transferred sequentially from CB of CdS to ZnIn_2S_4 to TiO_2 . Meanwhile the photogenerated holes on the VB side of TiO_2 directly move to ZnIn_2S_4 and then to VB of CdS . Thus, the electrons and holes move in a cascading fashion toward the surface of the platinum electrode (via external circuit) and the electrode-electrolyte interface. It was reported that the Fermi energy levels of individual components in the heterojunction tend to descend and rise up, which can form an electric field at the interface of the heterojunction system.⁴³ This also helps photoinduced electrons and holes to transfer thermodynamically from the conduction band of CdS to TiO_2/FTO .⁵⁰ As a result, recombination between electrons and holes is repressed, increasing the probability that electrons and holes will contribute to the oxidation-reduction reactions. The separated electrons arriving at the Pt electrode combine with the H^+ ions to produce H_2 . Additionally, holes transported at the heterojunction-electrolyte interface take part in oxidation reactions, in that, holes oxidize the SO_3^{2-} and S^{2-} ions

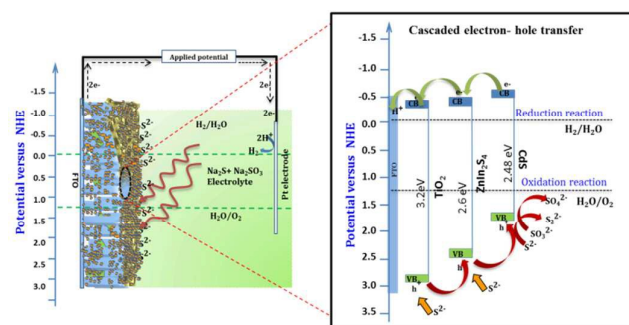


Fig. 9 Schematic mechanism of the cascading electron and hole transfer in the ternary $\text{CdS}/\text{ZnIn}_2\text{S}_4/\text{TiO}_2$ heterojunction system.

to form SO_4^{2-} and S_2^{2-} , respectively. The presence of excess S^{2-} ions in the reaction solution also stabilizes the photocatalyst surface because the formation of sulfur defects can be suppressed.⁵¹ However, small amounts of photogenerated charge carriers react with sacrificial reagents at the VB of each photoanode in the $\text{CdS}/\text{ZnIn}_2\text{S}_4/\text{TiO}_2$ architecture. Therefore, both CdS and ZnIn_2S_4 play significant roles in light absorption and facilitate the separation of electrons-holes, leading to improved photoelectrochemical performance.

Electrochemical characterization studies

To gain a deeper understanding about the charge transfer and recombination processes in $\text{ZnIn}_2\text{S}_4/\text{TiO}_2$, CdS/TiO_2 , and $\text{CdS}/\text{ZnIn}_2\text{S}_4/\text{TiO}_2$ heterojunction photoanodes, we measured and analyzed the electrochemical impedance spectra (EIS). EIS is a powerful tool for characterizing the performance of each component in PEC cells. It can be used to investigate the interior resistance, recombination, and charge transfer kinetics.⁵² Nyquist plots of $\text{ZnIn}_2\text{S}_4/\text{TiO}_2$, CdS/TiO_2 , and $\text{CdS}/\text{ZnIn}_2\text{S}_4/\text{TiO}_2$ heterojunction photoanodes are shown in Fig. 10. The measurements were carried out under light conditions at an applied forward bias of -0.1 V in order to study the interface resistance behavior of the different films. The $\text{ZnIn}_2\text{S}_4/\text{TiO}_2$, CdS/TiO_2 , and $\text{CdS}/\text{ZnIn}_2\text{S}_4/\text{TiO}_2$ heterojunction photoanodes were best-fitted to series resistance (R_s) and two RC-circuit models. The corresponding equivalent circuit model, shown in the inset of Fig. 10, was reported previously.^{53,54} The R_s comes from the sheet resistance of the substrate and the contact resistance in the external cell circuit. These RC circuits correspond to two major interfaces within photoanodes and predominantly consist of impedance elements that are assigned to bulk $\text{CdS}/\text{ZnIn}_2\text{S}_4/\text{TiO}_2$ and the $\text{CdS}/\text{ZnIn}_2\text{S}_4/\text{TiO}_2$ | electrolyte. R_f and CPE_1 represent the resistance and constant phase element of the $\text{CdS}/\text{ZnIn}_2\text{S}_4/\text{TiO}_2$ electrode and the FTO interface, respectively, while the charge transfer resistance (R_{ct}) and interfacial capacitance (CPE_2) are related to the photoanode/electrolyte interface. Fitting of the semicircles into Nyquist plots gives the impedance parameters and various

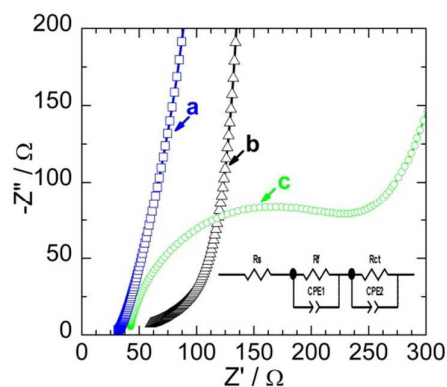


Fig. 10 Nyquist plots of (a) $\text{ZnIn}_2\text{S}_4/\text{TiO}_2$, (b) CdS/TiO_2 and (c) $\text{CdS}/\text{ZnIn}_2\text{S}_4/\text{TiO}_2$ photoanodes under 1 sun illumination (Z' and Z'' denote the real and imaginary parts respectively). The inset shows an equivalent circuit model used to fit the Nyquist plots.

resistance values, which are listed in Table 1. It can be clearly seen that R_f , which represents the interfacial resistance of the photoanode and FTO, is much lower in CdS/ZnIn₂S₄/TiO₂ compared to the pristine TiO₂, CdS/TiO₂, and ZnIn₂S₄/TiO₂ photoanodes. It is noted that the lower interfacial resistance can result in higher interfacial electron transfer, which is beneficial to the interfacial electron transfer from CdS to the TiO₂ layer through the ZnIn₂S₄ nanosheet.

Furthermore, the R_{ct} values drastically decrease upon the synergistic addition of CdS and ZnIn₂S₄ onto TiO₂, and the order of the R_{ct} values are measured as 31047 Ω (TiO₂) < 29634 Ω (CdS/TiO₂) < 21662 Ω (ZnIn₂S₄/TiO₂) < 363 Ω (CdS/ZnIn₂S₄/TiO₂). Generally, electrodes with large R_{ct} values cause slow charge transfer in the electrochemical system. The higher R_{ct} value of the CdS/TiO₂ heterojunction, relative to ZnIn₂S₄/TiO₂, confirms that it is irresponsible for the effective charge separation, despite the fact that CdS/TiO₂ absorbs the maximum amount of light. However, the lower R_{ct} value in ZnIn₂S₄/TiO₂ might be caused by the 2D morphology of ZnIn₂S₄, which can provide multiple electron-hole transfer sites for photoexcited charges, leading to an increase in the lifetime of electrons and holes. The most interesting result of the EIS fitting data is that the thin layer of ZnIn₂S₄ provides multiple pathways for carrying charges via its low resistive nanosheet structure and significantly affects the charge transfer characteristics of CdS/TiO₂ in CdS/ZnIn₂S₄/TiO₂ photoanode. These EIS results imply that both CdS and ZnIn₂S₄ can promote charge separation at any position (i.e., multi-steering charge transfer mechanism) in the photoanode and enhance the photocurrent ability.

Table 1. Parameters determined from EIS fitting of ZnIn₂S₄/TiO₂, CdS/TiO₂, and CdS/ZnIn₂S₄/TiO₂ photoanodes.

Samples/ Parameters	R_s Ω	R_f Ω	R_{ct} Ω	$C_{[CPE1]}$ μF	$C_{[CPE2]}$ μF
TiO ₂	33	1220	31047	0.4	8.3
CdS/TiO ₂	36	521	29634	530.5	8.6
ZnIn ₂ S ₄ /TiO ₂	31	257	21662	115.5	6.2
CdS/ZnIn ₂ S ₄ /TiO ₂	39	150	363	3.8	16.9

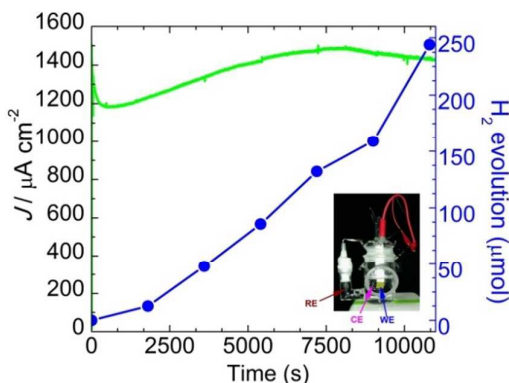


Fig. 11 Evolution of H₂ and photocurrent density as a function of time for the CdS/ZnIn₂S₄/TiO₂ photoanode under 100 mW cm⁻² light illumination. Inset shows a picture of the simple photoelectrochemical cell setup used for hydrogen generation (WE: working electrode, CE: counter electrode, and RE: reference electrode).

The EIS data is well correlated with PEC performance of CdS/ZnIn₂S₄/TiO₂ photoanode. The CdS/ZnIn₂S₄/TiO₂ photoanode was further tested for photoelectrochemical hydrogen generation at a bias of 0.1 V (vs. Ag/AgCl) in an electrolyte consisting of a solution of 0.1 M Na₂S and 0.02 M Na₂SO₃ under 1 sun illumination. Fig. 11 shows the photoelectrochemical hydrogen evolution analyzed by gas chromatography (GC) and the photocurrent density with respect to time. The picture of the simple photoelectrochemical cell setup used for hydrogen generation is shown in the inset of Fig. 11. It can be seen that the hydrogen evolution linearly increased with the solar light irradiation time and that the total amount of H₂ produced by the CdS/ZnIn₂S₄/TiO₂ photoanode was 248 μ mol after 3 h (82.6 μ mol h⁻¹). The photostability of the photoanode was also investigated during hydrogen production. It can be seen that, during photoelectrochemical hydrogen generation, the photocurrent density increased for the first 7000 s of irradiation before becoming stable. This increased current density can be attributed to the modification of the surface of CdS/ZnIn₂S₄/TiO₂; a similar phenomenon was previously reported for the TiO₂/RGO/Cu₂O heterostructure.²⁰ The long-term instability of the CdS/ZnIn₂S₄/TiO₂ photoanode necessitates future investigation into the optimization conditions (e.g., heat treatment, surface modifications, etc.), the mechanism of charge transfer, and the continued study of the factors that limit the photocurrent of CdS/ZnIn₂S₄/TiO₂ photoanodes for solar hydrogen generation.

Conclusions

In conclusion, we have successfully developed a highly efficient, visible light-active, ternary CdS/ZnIn₂S₄/TiO₂ architecture on FTO via the hydrothermal synthesis of TiO₂ nanorods, CdS nanograins, and ZnIn₂S₄ nanosheets. Both the CdS nanograins and the ZnIn₂S₄ nanosheets in the CdS/ZnIn₂S₄/TiO₂/FTO photoanode can aid in light absorption and exhibited efficient hierarchical cascading during electron and holes transfer. The CdS/ZnIn₂S₄/TiO₂ architectures demonstrated an enhanced photocurrent density (1.4 mA cm⁻², AM1.5), which is 5.6 times higher than that of pristine ZnIn₂S₄/TiO₂ and nearly 2.3 times higher than that of CdS/TiO₂. EIS data also showed that the CdS/ZnIn₂S₄/TiO₂ heterostructure provides the lowest charge-transfer resistance amongst the photoanodes that were studied. The relatively higher photoelectrochemical performance of the CdS/ZnIn₂S₄/TiO₂ heterostructure is mainly associated with (i) the significantly broadened visible light absorption capacity of the CdS layer and (ii) the highly efficient cascading that occurs during electron and hole transfer, which reduces recombination during the transfer process. This work not only demonstrates that ZnIn₂S₄ and CdS are promising candidates for the development of high efficient architectures, but also opens new possibilities to provide insight into the design of new modified photoanodes with high activity for solar hydrogen generation.

Acknowledgements

This research was supported by the Basic Science Research Programs through the National Research Foundation of Korea (NRF), funded by the Ministry of Education, Science, and Technology (2012R1A6A3A04038530), as well as the Korea Ministry of Environment (MOE) as Public Technology Program based on Environmental Policy (2014000160001).

References

- B. B. Kale, J. O. Baeg, S. M. Lee, H. Chang, S. J. Moon and C. W. Lee, *Adv. Funct. Mater.*, 2006, **16**, 1349.
- Y. Yu, G. Chen, G. Wang and Z. Lv, *Int. J. Hydrogen Energ.*, 2013, **38**, 1278.
- Y. B. Li, Z. F. Liu, Y. Wang, Z. C. Liu, J. H. Han and J. Ya, *Int. J. Hydrogen Energ.*, 2012, **37**, 15029.
- A. Valdes, J. Brillet, M. Grätzel, H. Gudmundsdottir, H. A. Hansen, H. Jonsson, P. Klupfel, G. Kroes, F. Formal, I. C. Man, R. S. Martins, J. K. Nørskov, J. Rossmeisl, K. Sivula, A. Vojvodic and M. Zach, *Phys. Chem. Chem. Phys.*, 2012, **14**, 49.
- P. S. Shinde, A. Annamalai, J. Y. Kim, S. H. Choi, J. S. Lee and J. S. Jang, *J. Phys. Chem. C*, 2015, **119**, 5281.
- W. Kim, T. Tachikawa, D. Monllor-Satoca, H. Kim, T. Majima and W. Choi, *Energy Environ. Sci.*, 2013, **6**, 3732.
- G. C. De, A. M. Roy and S. S. Bhattacharya, *Int. J. Hydrogen Energ.*, 1995, **20**, 127.
- P. Sheng, W. Li, J. Cai, X. Wang, X. Tong, Q. Cai and C. A. Grimes, *J. Mater. Chem. A*, 2013, **1**, 7806.
- L. M. Peter, D. J. Riley, E. J. Tull and K. G. U. Wijayantha, *Chem. Commun.*, 2002, **10**, 1030.
- C. H. Chang and Y. L. Lee, *Appl. Phys. Lett.*, 2007, **91**, 0535031.
- W. Wu, R. Lin, L. Shen, R. Liang, R. Yuan and L. Wu, *Phys. Chem. Chem. Phys.*, 2013, **15**, 19422.
- N. Serpone, E. Borgarello and M. Grätzel, *J. Chem. Soc., Chem. Commun.*, 1984, 342.
- D. Robert, *Catal. Today*, 2007, **122**, 20.
- S. Biswas, M. F. Hossain and T. Takahashi, *Thin Solid Films*, 2008, **517**, 1284.
- S. Chen, M. Paulose, C. Ruan, G. K. Mor, O. K. Varghese, D. Kouzoudis and C. A. Grimes, *J. Photochem. Photobiol. A: Chem.*, 2006, **177**, 177.
- Z. Mei, S. Ouyang, D. M. Tang, T. Kako, D. Golberg, and J. Ye, *Dalton Trans.*, 2013, **42**, 2687.
- N. Romeo, A. Dallaturca, R. Braglia and G. Sberveglieri, *Appl. Phys. Lett.*, 1973, **22**, 21.
- M. Zhou, X. W. Lou and Y. Xie, *Nano Today*, 2013, **8**, 598.
- J. H. Yang, K. Walczak, E. Anzenberg, F. M. Toma, G. B. Yuan, J. Beeman, A. Schwartzberg, Y. J. Lin, M. Hettick, A. Javey, J. W. Ager, J. Yano, H. Frei and L. D. Sharp, *J. Am. Chem. Soc.*, 2014, **136**, 6191.
- W. Fan, X. Yu, H. C. Lu, H. Bai, C. Zhang, and W. Shi, *Appl. Catal. B-Environ.*, 2016, **181**, 7.
- Q. Huang, F. Kang, H. Liu, Q. Li and X. Xiao, *J. Mater. Chem. A*, 2013, **1**, 2418.
- H. Kim and B. L. Yang, *Int. J. Hydrogen Energ.*, 2015, **40**, 5807.
- B. Liu and E. S. Aydil, *J. Am. Chem. Soc.*, 2009, **131**, 3985.
- C. Cao, C. Hu, X. Wang, S. Wang, Y. Tian and H. Zhang, *Sens. Actuators B*, 2011, **156**, 114.
- S. Peng, P. Zhu, V. Thavasi, S. G. Mhaisalkar and S. Ramakrishna, *Nanoscale*, 2011, **3**, 2602.
- Y. Xie, L. Wei, G. Wei, Q. Li, D. Wang, Y. Chen, S. Yan, G. Liu, L. Mei, and J. Jiao, *Nanoscale Res. Lett.*, 2013, **8**, 1881.
- J. Han, Z. Liu, K. Guo, B. Wang, X. Zhang and T. Hong, *Appl. Catal. B*, 2015, **163**, 179.
- F. Fang, L. Chen, Y. B. Chen and L. M. Wu, *J. Phys. Chem. C*, 2010, **114**, 2393.
- B. Chai, T. Y. Peng, P. Zeng and X. H. Zhang, *Dalton Trans.*, 2012, **41**, 1179.
- G. Yang, B. Yang, T. Xiao and Z. Yan, *Appl. Surf. Sci.*, 2013, **283**, 402.
- M. Marychurch and G. C. Morris, *Surf. Sci.*, 1985, **154**, L251.
- J. Chastain, R. C. King and J. F. Moulder, *Handbook of X-ray photoelectron spectroscopy: a reference book of standard spectra for identification and interpretation of XPS data*, Physical Electronics, Eden Prairie, Minnesota, 1995.
- Y. Kim, H.B. Kim and D. J. Jang, *J. Mater. Chem. A*, 2014, **2**, 5791.
- J. Hou, C. Yang, H. Cheng, Z. Wang, S. Jiao and H. Zhu, *Phys. Chem. Chem. Phys.*, 2013, **15**, 15660.
- J. Li, M. W. G. Hoffmann, H. Shen, C. Fabreg, J. D. Prades, T. Andreu, F. H. Ramirez and S. Mathur, *J. Mater. Chem.*, 2012, **22**, 20472.
- Y. J. Chi, H. G. Fu, L. H. Qi, K. Y. Shi, H. B. Zhang and H. T. Yu, *J. Photochem. Photobiol. A: Chem.*, 2008, **195**, 357.
- T. C. Dang, D. L. Pham, H. C. Le, and V. H. Pham, *Adv. Nat. Sci.: Nanosci. Nanotechnol.*, 2010, **1**, 0150021.
- F. P. Gökdemir, V. E. Yüzbaşıoglu, B. Keskin, O. Özdemir and K. Kutlu, *Adv. Mat. Lett.*, 2014, **5**, 367.
- C. Lu, L. Zhang, Y. Zhang, S. Liu, G. Liu, *Appl. Surf. Sci.*, 2014, **319**, 278.
- Q. Liu, H. Lu, Z. Shi, F. Wu, J. Guo, K. Deng and L. Li, *ACS Appl. Mater. Interfaces*, 2014, **6**, 17200.
- J. Yu, Y. Wang and W. Xiao, *J. Mater. Chem. A*, 2013, **1**, 10727.
- I. B. Assaker, M. Gannouni, J. B. Naceur, M. A. Almessiere, A. L. Al-Otaibi, T. Ghrib, S. Shen, and R. Chtourou, *Appl. Surf. Sci.*, 2015, **351**, 927.
- J. Zhou, L. Yin, H. Li, Z. Liu, J. Wang, K. Duan, S. Qu, J. Weng, B. Feng, *Mater. Sci. Semicond. Process.*, 2015, **40**, 107.
- F. X. Xiao, J. Miao, H.Y. Wang and B. Liu, *J. Mater. Chem. A*, 2013, **1**, 12229.
- Y. Zhu, R. Wang, W. Zhang, H. Ge, L. Li, *Appl. Surf. Sci.*, 2014, **315**, 149.
- F. Wang, Y. Wang, X. Zhan, M. Safdar, J. Gong and J. He, *Cryst. Eng. Comm.*, 2014, **16**, 1389.
- U. Bach, D. Lupo, P. Comte, J. E. Moser, F. Weissörte, J. Salbeck, H. Spreitzer and M. Grätzel, *Nature*, 1998, **395**, 583.
- G. Zhang, B. Lin, W. Yang, S. Jiang, Q. Yao, Y. Chen and B. Gao, *RSC Adv.*, 2015, **5**, 5823.
- H. Zhang, X. Zuo, H. Tang, G. Li and Z. Zhou, *Phys. Chem. Chem. Phys.*, 2015, **17**, 6280.
- M. Humayun, A. Zada, Z. Li, M. Xie, X. Zhang, Y. Qu, F. Raziq and L. Jing, *Appl. Catal. B: Environ.*, 2016, **180**, 219.
- I. Tsuji, H. Kato, H. Kobayashi and A. Kudo, *J. Am. Chem. Soc.*, 2004, **126**, 13406.
- H.J. Kim, H. D. Lee, C. S. S. P. Kumar, S. S. Rao, S. H. Chung and D. Punnoose, *New J. Chem.*, 2015, **39**, 4805.
- J. Y. Kim, G. Magesh, D. H. Youn, J. W. Jang, J. Kubota and K. Domen, *Sci. Rep.*, 2013, **3**, 2681.
- B. Chen, N. Zhao, L. Guo, F. He, C. Shi, C. He, J. Li and E. Liu, *Nanoscale*, 2015, **7**, 12895.

Graphical Abstract

